PHYSICAL REVIEW A VOLUME 50, NUMBER 4 OCTOBER 1994

Spatial distortions of laser pulses in coherent on-resonance propagation: Large-scale self-focusing

J. de Lamare
COGEMA and Commissariat à l'Energie Atomique, Centre d'Etudes Nucléaires de Saclay, DCC/DPE/SPEA, 91 191 Gif-sur-Yvette, France

M. Comte
Commissariat à l'Energie Atomique, Centre d'Etudes Nucléaires de Saclay, DCC/DPE/SPEA, 91 191 Gif-sur-Yvette, France

Ph. Kupecek
Université Pierre et Marie Curie and Commissariat à l'Energie Atomique, Centre d'Etudes Nucléaires de Saclay, DCC/DPE/SPEA, 91 191 Gif-sur-Yvette, France

(Received 18 March 1994)

When cylindrical symmetry is assumed, a numerical study of coherent on-resonance self-focusing of laser pulses in atomic media reveals a well-defined dependence on the interaction's parameters for the focusing distance and the maximal on-axis energy density reached at the focus. We interpreted this focusing to be the result of a diaphragm effect at the edge of the pulse. This can be readily explained by considering the transverse dependence of local self-induced transparency phenomena first described by McCall and Hahn [Phys. Rev. Lett. **18**, 908 (1967); Phys. Rev. **183**, 457 (1969)]. From this interpretation and the well-known Maxwell-Bloch equations, we derived a theoretical quantitative model for coherent on-resonance large-scale self-focusing, that is to say, focusing of the beam as a whole. Our main results include the above-mentioned exact parametric dependence for the focusing distance, as well as predictions about the ratios of on-axis energy densities and pulse transverse sizes between the input and focus planes. All of these predictions appear to corroborate the results of an experiment on a ^{169}Tm vapor.

PACS number(s): 42.50.Md, 42.25.Bs, 42.65.Jx, 32.80.−t

I. INTRODUCTION

Since 1965, transverse phenomena have been emphasized in works dealing with self-focusing or defocusing of optical pulses, but these works usually have been concerned with the effects of nonresonant nonlinearities in the quasi-steady-state limit, as in common transparent media [1–3]. Self-lensing due to an intensity-dependent index of refraction explains the main part of these phenomena. A review paper by Akhmanov, Sokhurov, and Khokhlov [4] contains a bibliography of work in this area, which has been completed by the more recent contributions of Harter and Boyd [5] and Braun, Faucheux, and Libchaber [6] (see also [7]). Wong and Shen investigated theoretically and experimentally the transient limit of these effects, when the pulse duration τ_p is shorter than or comparable to the relaxation time τ of the refractive index [8,9].

In the steady-state case of an on-resonance cw laser interacting with an atomic medium, a relatively smooth self-focusing (compared with the nonresonant nonlinear case) may also occur. A complete investigation of this phenomenon has been made by Boshier and Sandle [10], Tai *et al.* [11], and LeBerre *et al.* [12]. It is viewed as a consequence of Fresnel diffraction induced by absorption on the wings of the laser-beam transverse profile.

Since the publication of the pioneering work of McCall and Hahn [13], on-resonance propagation of optical pulses in absorbers in the coherent regime, that is to say, when τ_p is shorter than all the relaxation times of the medium, has been the subject of numerous studies [14–17]. Nonlinear transmission and temporal reshaping effects such as pulse breakup, pulse delays, and peak amplification have been observed and successfully compared with theoretical predictions [18]. In thick absorbers, however, transverse effects such as self-focusing can dominate pulse reshaping, and the complete set of Maxwell-Bloch equations—including radial variations and time-dependent phase—is required for any analytical description. Because of the complexity of this system, there has been up to now no theoretical quantitative model for coherent on-resonance large-scale self-focusing (LSSF), but only numerical simulations that assume cylindrical symmetry and qualitative interpretations. Wright and Newstein [19] attributed this self-focusing to a transverse energy flow they found to be proportional to the local-field intensity and phase profile radial curvature. Gibbs *et al.* [20] pointed out that self-focusing is predicted numerically for $F=\lambda/4\pi r_p^2\alpha$ ranging between 10^{-4} and 10^{-2} (in which λ is the optical wavelength, r_p the input pulse transverse characteristic radius, and α the "low-intensity" gain of the medium, so that F is the inverse of a Fresnel number), for distances L such that $\alpha L>5$. Focusing is attributed to a diffraction-induced inward flow of energy from the outer rings which, due to the self-induced-transparency (SIT) reshaping effects, undergo larger delays than the more intense inner ones. This argument was repeated later in the numerous numerical studies made by Mattar [21,22].

In the present paper, we give the main results of a systematic numerical study of the focusing effect (Sec. II), the interpretation of which led us to a quantitative theoretical model (Sec. III). Both numerical and theoretical descriptions are compared with the results of an experiment involving nanosecond dye laser pulses interacting with a degenerate inhomogeneously broadened two-level system provided by a fundamental transition in a ^{169}Tm vapor (Sec. VI). The influence of Zeeman degeneracy and detuning from resonance is discussed in Sec. V. Finally, Sec. VI is a summary of the main results.

II. COMPUTER SOLUTIONS

A. Field and material system equations

In our study, the electric field is assumed to be linearly polarized transverse to the direction of propagation, z, and of the form

$$\mathcal{E}=\mathrm{Re}\{E(r,z,t)\exp[i(kz-\omega t)]\}\ , \tag{1}$$

in which

$$k=\frac{\omega}{c} \tag{2}$$

is the wave-vector modulus, ω is the optical circular frequency, c is the vacuum speed of light, r is the transverse radial coordinate, and E is the electric-field complex envelope. We have chosen to neglect the contribution to the atomic response of possible nonresonant buffer gas transitions. The remaining resonant part of the atomic response is taken to be of the following form:

$$\mathcal{P}=\mathrm{Re}\{P(r,z,t)\exp[i(kz-\omega t)]\}\ , \tag{3}$$

in which P is its complex envelope and can be written as follows [23]:

$$P=N\mu(u-iv)\ , \tag{4}$$

in which N is the atomic concentration and μ is the projection of the mean dipole-moment operator on the field polarization direction. (u,v) are real functions, solutions of the well known Bloch equations that describe the statistical time evolution of both the atomic polarization and population inversion w:

$$\begin{aligned}\frac{\partial u}{\partial t}&=-\Delta\omega v+\mathrm{Im}(\Omega)w\ ,\\ \frac{\partial v}{\partial t}&=\Delta\omega u+\mathrm{Re}(\Omega)w\ ,\\ \frac{\partial w}{\partial t}&=-[v\mathrm{Re}(\Omega)+u\mathrm{Im}(\Omega)]\ ,\end{aligned} \tag{5}$$

in which

$$\Delta\omega=\omega-\omega_0 \tag{6}$$

is the detuning between the laser and atomic resonance circular frequencies and

$$\Omega=\frac{\mu E}{\hbar} \tag{7}$$

is the Rabi circular frequency. In atomic vapors, transitions are generally Doppler-broadened and we have taken, respectively, $g(\Delta\omega)$ and $\Delta\omega_{\mathrm{dop}}$ as the corresponding normalized spectral distribution of the absorbers and its full width at half maximum. Taking this broadening into account leads to putting $P=N\mu(U-iV)$ in which (U,V) is the full atomic response, calculated by integration of (u,v) over $g(\Delta\omega)$. When Ω is real (and since w must not depend on the sign of $\Delta\omega$), one can easily deduce from the above Bloch equations that u and v are, respectively, odd and even functions of $\Delta\omega$ [24]. Consequently [$g(\Delta\omega)$ being an even function], $U=0$ when the laser is on resonance. In this limit only absorption and stimulated emission are important.

E and P are assumed to vary slowly with respect to z and t for distances and durations comparable to the optical wavelength and period. The simplest form of the paraxial wave equation [25] in cylindrical coordinates [23] is obtained in a frame traveling at the velocity of light in vacuum, and in a dimensionless form, as follows:

$$\frac{\partial e}{\partial\eta}-iF\Delta_{\rho}e=(V+iU)(\rho,\eta,\tau)\ , \tag{8}$$

with

$$V+iU(\rho,\eta,\tau)=\frac{1}{2\pi}\int(v+iu)(\rho,\eta,\tau,\delta)\times\exp\left[-4\ln2\left[\frac{\delta}{D}\right]^{2}\right]d\delta\ , \tag{9}$$

in which $F=(\lambda/4\pi r_p^2\alpha)$, $\alpha=(2\pi^2\mu^2N/\varepsilon_0\lambda\hbar)g(0)$ is the longitudinal low-intensity gain, $g(0)=[2(\ln2)^{1/2}/\Delta\omega_{\mathrm{dop}}\pi^{1/2}]$ [consequently $g(0)$ is proportional to λ], and in which we define the dimensionless quantities corresponding to the time, longitudinal and radial coordinates, Rabi frequency, frequency detuning, and $\Delta\omega_{\mathrm{dop}}$ as, respectively,

$$\begin{aligned}&\tau=t/\tau_p,\quad \eta=\alpha z,\quad \rho=r/r_p,\quad e=\frac{\mu E}{\hbar}\tau_p\ ,\\ &\delta=\Delta\omega\tau_p,\quad D=\Delta\omega_{\mathrm{dop}}\tau_p\ .\end{aligned} \tag{10}$$

Δ_p is the expression of the Laplacian transverse in dimensionless radial coordinate $(1/\rho)(\partial/\partial\rho)[\rho(\partial/\partial\rho)]$. As can be seen, the full dimensionless problem (8)+(9) depends only on two parameters, F and D. F characterizes the respective predominance of either temporal reshaping or of transverse distortions due to diffraction. When F is comparable to or larger than 1, the preponderant phenomenon is a global divergence of the whole beam and no self-focusing can be expected. In what follows, we limit ourselves to the case in which the pulse spectral width is smaller than the inhomogeneous broadening, that is to say, $D>1$. It corresponds to the very common situation of a smooth pulse whose length is of the order of a few ns or more, propagating in an atomic vapor. It is implied that all the incident pulse photons can interact with resonant absorbers.

B. Numerical parametric study of self-focusing

A typical self-focusing numerical result is given in Fig. 1, with the on-axis energy density H (J/cm^2) a function of propagation distance. We characterize this result by the ratio of on-axis energy densities between the input and focus planes, $H_{\max}/H_0$, and the distance between these planes, L_{foc}. The decreasing part of the curve beyond L_{foc} (dashed line) may be interpreted as a consequence of a combined effect of absorption and defocusing, depending on the interaction's parameters. We do not discuss this point further in this work.

The most striking numerical result is that L_{foc} is strictly proportional to the transverse size of the input pulse, as shown in Fig. 2. From this significant result, a simple dimensional analysis of Eq. (8) (see Appendix A) leads to the following prediction:

$$L_{\mathrm{foc}} \propto \frac{r_p}{\sqrt{\alpha\lambda}} , \qquad (11)$$

which was fully confirmed numerically. Since α does not depend on λ, the above result indicates directly the full dependence of L_{foc} on λ. We also found numerically that L_{foc} increases slightly with the dimensionless initial Rabi frequency, something which we shall explain in Sec. III C. Moreover, it doesn't depend significantly on D.

Concerning $H_{\max}/H_0$, we found its parametric dependence to match nicely as follows:

$$\frac{H_{\max}}{H_0} \propto \frac{r_p^{3/2}\alpha^{3/4}}{\lambda^{3/4}} . \qquad (12)$$

C. Temporal reshaping and self-focusing; dependence on initial optical area

A significant concept in the field of coherent resonant interaction is the optical area, defined by

$$\Theta = \int_{-\infty}^{+\infty} \Omega(t)dt . \qquad (13)$$

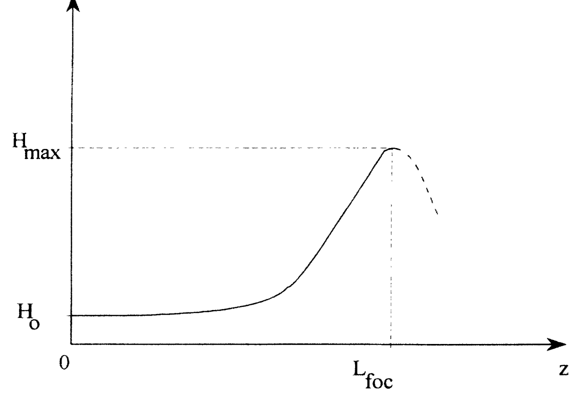

FIG. 1. Characterization of self-focusing by the longitudinal evolution of the on-axis energy density.

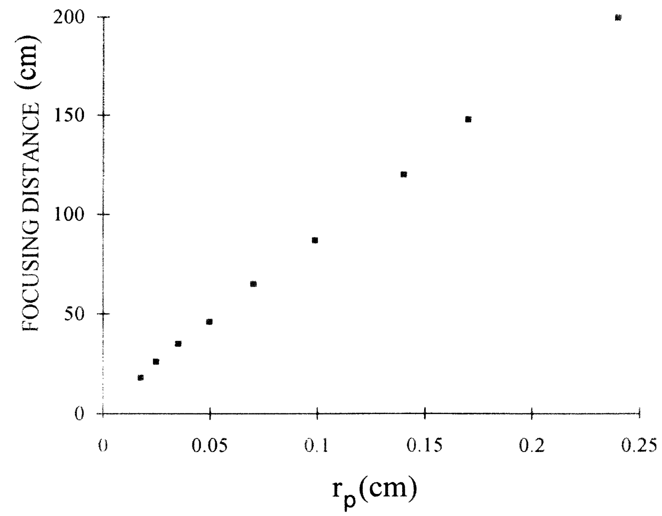

FIG. 2. Proportionality of L_{foc} to the transverse size of the input pulse. Other numerical data: $\alpha=0.41$ rad cm^{-1}; $\lambda=0.64$ μm; $D=25$ rad; both transverse and temporal profiles of the input 2.6π pulse are Gaussian.

The previous results were obtained for an input pulse whose energy corresponds to nearly 2π optical area. In the plane-wave SIT approximation, such a pulse is expected to undergo temporal reshaping. As predicted by the area theorem [Ref. 13(b), Eq. (3)],

$$\frac{d\Theta}{dz} = -\frac{\alpha}{2}\sin\Theta(z) , \qquad (14)$$

it evolves progressively into a 2π-sech stable profile on a distance proportional to $1/\alpha$. Shore investigated the dependence of this effect on the initial temporal profile, giving numerical formulas for the distance required by 2π pulses of various initial shapes to reach a stable 2π-sech form [26]. In what follows, we shall posit L_{res} as the characteristic length of temporal reshaping (L_{res} is proportional to $1/\alpha$). For an initial area ranging between $(2k-1)\pi$ and $(2k+1)\pi$, in which k is an integer and $k \geq 1$, the pulse is expected to reach a stable form of k successive 2π-sech pulses, on a distance of the order of L_{res}. Although not yet theoretically demonstrated in the general case [27], this behavior can be observed numerically and experimentally [13,18]. Temporal reshaping of experimental pulses must be described more completely by including the transverse dimension. Let us consider the example of an initial pulse whose on-axis area ranges between 5π and 6π, and whose energy transverse profile is monotonically decreasing. The qualitative evolution of its spatiotemporal-intensity profile is described in Fig. 3 and can be obtained in the following manner. Part 1 of the initial pulse (a), corresponding to initial optical areas smaller than π, is completely absorbed. Part 2, corresponding to optical areas ranging between π and 3π, reach a stable form corresponding to a single 2π pulse. Part 3, corresponding to optical areas ranging between 3π and 5π, reach a stable form of two successive 2π

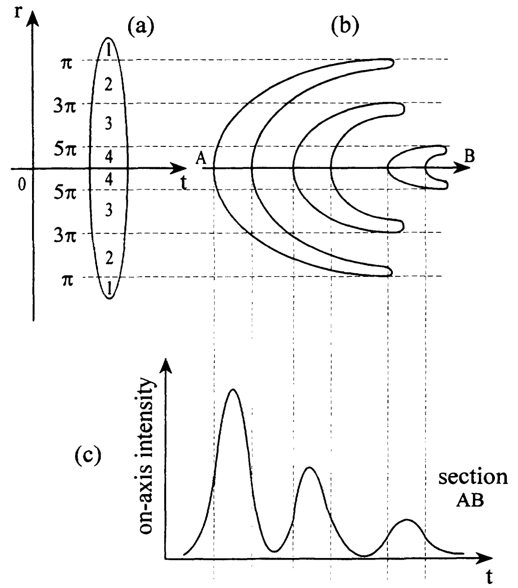

FIG. 3. Qualitative description of the temporal reshaping phenomenon and its dependence on the radial coordinate. The case of an input pulse whose on-axis optical area ranges between 5π and 7π. (a) Spatiotemporal profile of the input pulse. (b) Spatiotemporal profile of the "reshaped" pulse. (c) Section AB of (b) showing the temporal evolution of the on-axis intensity of the reshaped pulse.

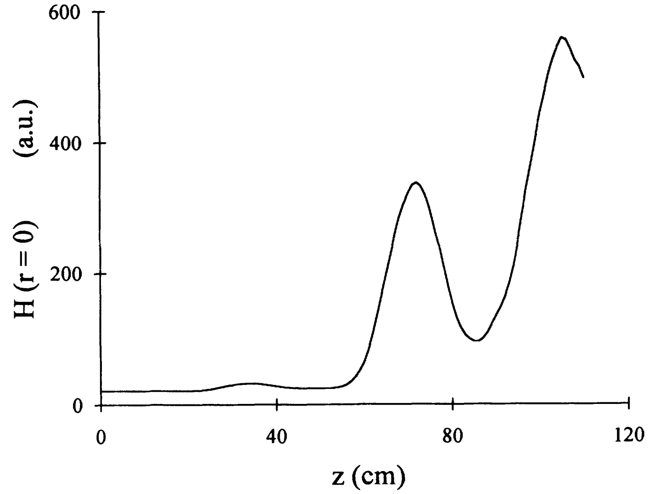

FIG. 4. Longitudinal evolution of the on-axis energy density of a 5.5π pulse. The case in which $L_{\text{res}} < L_{\text{foc}}$. Successive foci are well separated. Numerical data: $F = 2\times10^{-3}$ rad^{-1}, $\alpha = 0.26$ rad cm^{-1}, $D = 24$ rad.

pulses. Part 4, corresponding to optical areas larger than 5π, reach a stable form of three successive 2π pulses. Since local delays are proportional to the inverse of the local initial Rabi frequency, the initial pulse (a) evolves progressively in a succession (b) of three crescent-shaped pulses [28], whose on-axis individual areas are 2π (as previously explained). The temporal evolution of the on-axis intensity corresponding to section AB in (b) is represented in (c): one can recognize the typical result of one-dimensional temporal reshaping. It is noteworthy that each individual pulse in (b) has its own transverse characteristic radius, corresponding to a particular value of F. Accordingly, we can see from the prediction (11) that each pulse is expected to undergo self-focusing at its own distance (or is not expected to focus if its characteristic radius is too small, that is to say, if the corresponding value of F is too large). This behavior is shown in Fig. 4, where the longitudinal evolution of the on-axis energy density of an input 5.5π pulse is represented. We can barely distinguish a first maximum, just before 40 cm, corresponding to the smooth focusing of the third 2π pulse of Fig. 3(b): its characteristic radius is small and, moreover, it does not really undergo self-focusing. Then two successive foci appear that correspond, respectively, to the focusing of the second and first pulses of Fig. 3(b). The description we have just made is valid only if self-focusing does not prevent SIT phenomena from occurring. A simple and obvious condition for SIT predictions to remain valid in spite of self-focusing is that $L_{\text{res}} \ll L_{\text{foc}}$. This was fulfilled in the case of Fig. 4. Assuming only a smaller value of the characteristic radius of the input pulse than in the case presented in Fig. 4, the other parameters unchanged (so that L_{res} is of the same order as L_{foc}), we obtain the result presented in Fig. 5. SIT predictions are greatly affected by self-focusing, and pulse breakup followed by successive self-focusing of the individual pulses is not predicted in such cases. We see that individual foci are not as well separated as they are in the case of Fig. 4. This point was confirmed experimentally (see Sec. IV). Let us finally remark that the predominance of either temporal reshaping or self-focusing effect is characterized by $L_{\text{res}}/L_{\text{foc}}$, which is only $\sqrt{F}$.

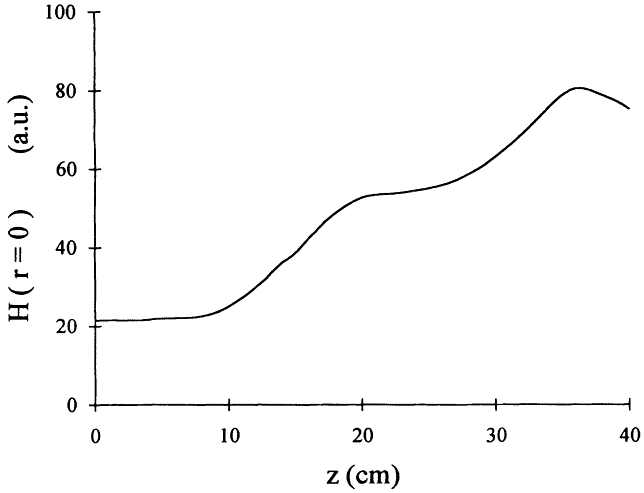

FIG. 5. Longitudinal evolution of the on-axis energy density of a 5.5π pulse. The case in which $l_{\text{res}} \approx L_{\text{foc}}$. Successive foci are not as well separated as in the case of Fig. 4. Numerical data: $F = 3.4\times10^{-2}$ rad^{-1}, $\alpha = 0.26$ rad cm^{-1}, $D = 24$ rad.

D. Diaphragm effect on the wings of the pulse

Figure 6 shows the evolution of the energy density transverse profile of an input on-axis 2.5π pulse, as propagation distances increase. With $F=3.4\times10^{-4}$, it corresponds to the case in which $L_{\text{foc}} \gg L_{\text{res}}$. Both of the input transverse and temporal profiles are Gaussian. An absorption singularity on the pulse wing can clearly be distinguished. This sort of diaphragm effect is initiated from a transverse position which corresponds to a local input area of π. We shall indicate this position as r_π (respectively, ρ_π in its dimensionless form) in the following part of this paper. Moreover, one can observe that transverse perturbations appear and propagate radially in an inward direction. In this case, focusing is predicted at 200 cm. Such behavior can be systematically observed in numerical simulations. However, for increasing values of F, global divergence of the beam begins to compete with absorption on the wings, this progressively leading to smoothing in the same way both the diaphragm and self-focusing effects, as is shown in Fig. 7, where $F=3.4\times10^{-2}$. A full explanation of the diaphragm effect requires the area theorem and some more precise results from Bloch equations. Let us note that an analogy between the absorption on the wings of the pulse and a diaphragm effect had already been suggested by Slusher and Gibbs [18]. We show in the following section that this effect leads to self-focusing by generating transverse perturbations that can propagate toward the axis. A quantitative model for LSSF can be derived from this simple interpretation.

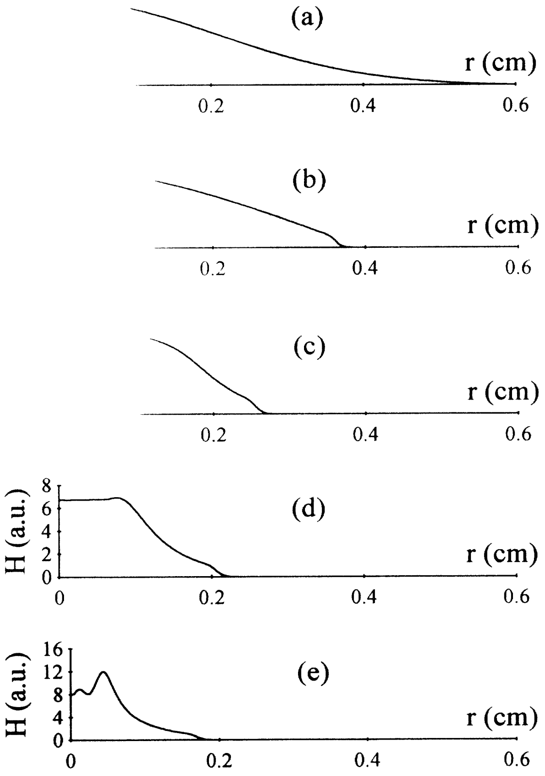

FIG. 6. Evolution of the transverse profile of the energy. The case in which $L_{\text{res}} \ll L_{\text{foc}}$. (a) $z=0$; (b) $z=40$ cm; (c) $z=120$ cm; (d) $z=150$ cm; (e) $z=170$ cm. Numerical data: $F=3.4\times10^{-4}$ rad^{-1}, $\alpha=0.26$ rad cm^{-1}, $D=24$ rad, input 2.4π pulse.

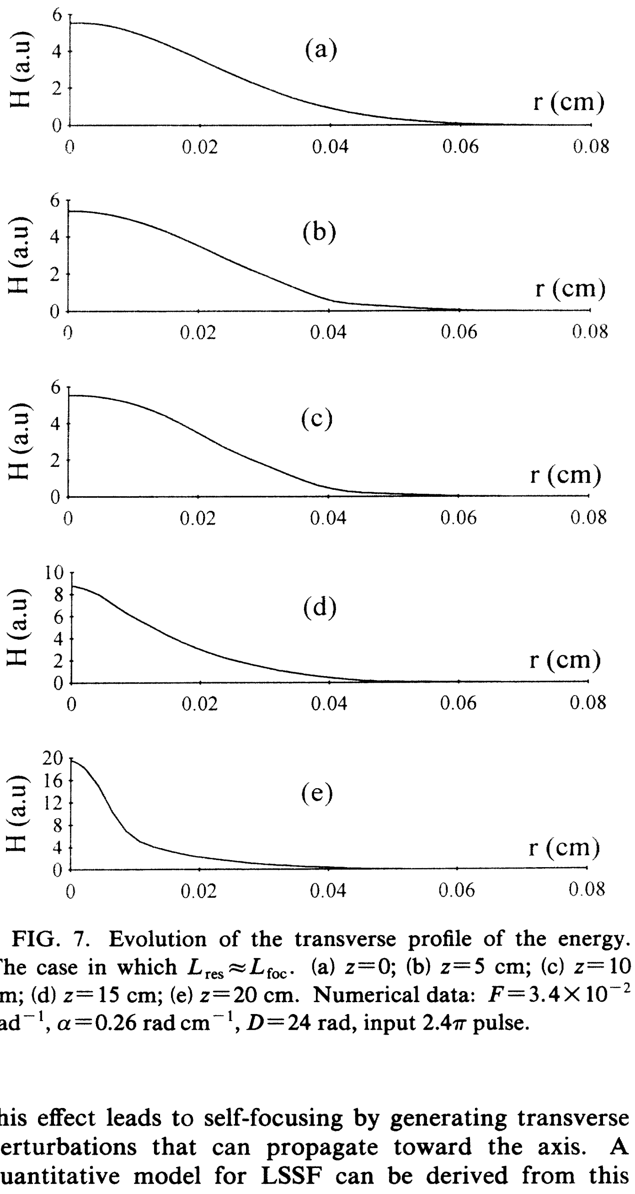

FIG. 7. Evolution of the transverse profile of the energy. The case in which $L_{\text{res}} \approx L_{\text{foc}}$. (a) $z=0$; (b) $z=5$ cm; (c) $z=10$ cm; (d) $z=15$ cm; (e) $z=20$ cm. Numerical data: $F=3.4\times10^{-2}$ rad^{-1}, $\alpha=0.26$ rad cm^{-1}, $D=24$ rad, input 2.4π pulse.

III. THEORY

A. Progressive diaphragm effect and area theorem

When there is no inhomogeneous broadening, the atomic response to an incident resonant electric field is given by the following solution of the Bloch equations [24]:

$$v(t) = -\sin\theta(t) \,, \tag{15a}$$

$$u(t) = 0 \,, \tag{15b}$$

in which

$$\theta(t) = \int_{-\infty}^{t} \Omega(u)\,du \tag{16}$$

is the partial optical area. The medium reaction is then oscillating. Stimulated emission processes ($v>0$), corresponding to a gain for the electric field [see Sec. II, Eq.

(8)], follow after absorption ($v<0$), in cycles whose duration is exactly, for a field of constant amplitude, the Rabi period. The number of these cycles is directly proportional to the input-pulse optical area. We compare, in Fig. 8, the respective atomic responses to inputs 2π (full line) and π (dashed line) Gaussian pulses. the 2π pulse undergoes absorption during the first half (that is, before time t_0) but the absorbed photons are completely radiated back to it during the second half, so that it can propagate without significant loss. As for the π pulse, we see that it is only absorbed (as with any pulse whose input area is smaller than π). This simplified description leads to a good qualitative interpretation of the correspondence between input area and transmission rate in the coherent regime [13,18]. Keeping this correspondence in mind, it is easy to understand that a 2π on-axis input pulse with a monotonically decreasing transverse energy profile can be expected to undergo a progressive diaphragm effect on its wings. More precisely, we know that this effect is initiated at the transverse position in which the local input area is π, as was shown numerically (see Fig. 6). We also know from the results presented in Fig. 8 that this effect occurs essentially during the second temporal part of the pulse (in other words, at the "tail" of the pulse, a conclusion that is in accord with that of Mattar [21]). The dependence of diaphragm characteristics on the propagation distance can be extrapolated from a graphic representation of the area theorem (represented in Fig. 9), which we have taken from Ref. [13(b)]. One can see that the longitudinal evolution of an area slightly below π is very close to the graphic representation of the first half of a sinusoidal function whose wavelength would be $8\pi/\alpha$. This leads to the main point of our LSSF model: on the one hand, we consider that the longitudinal evolution of the medium-induced "diaphragm" can be described by a sinusoidal behavior. We express this with a wave packet whose central wavelength $\lambda_{\parallel}$ is $8\pi/\alpha$. On the other hand, we maintain that the resulting transverse perturbations of the electric field (qualitatively, as in the Fresnel diffraction regime) exhibit the same longitudinal behavior and lead to self-focusing.

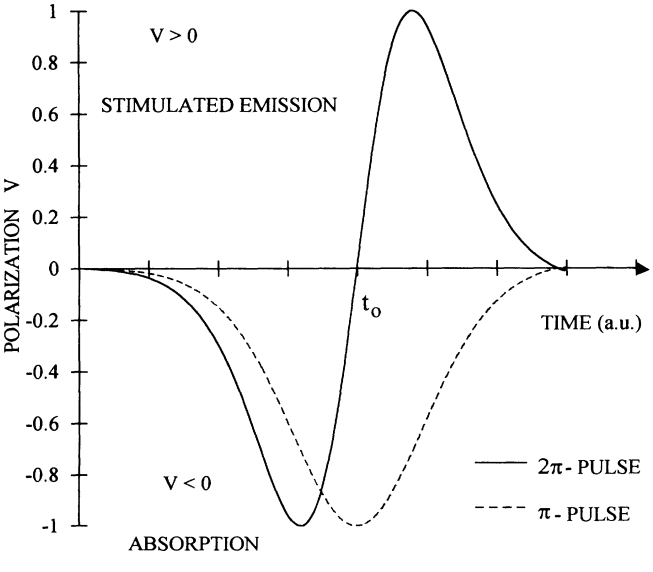

FIG. 8. Compared atomic responses to input 2π and π pulses. Pulses are Gaussian, simultaneous, and of equal durations. Inhomogeneous broadening is not taken into account.

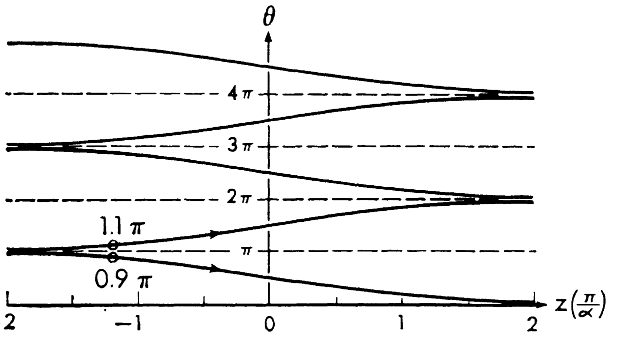

FIG. 9. Pulse area plots of SIT area theorem. Branch solutions to Eq. (14) are plotted [after Ref. 13(b)].

This interpretation agrees substantially, in its theory, with the works of Lit and Tremblay on laser-beam multiple-aperture focusing [29], which had predicted much stronger effects than in the simple Fresnel case of a single material diaphragm in which the maximum on-axis value of $H_{\max}/H_0$ is 4.

B. Analytical model

Our LSSF model is based on a perturbational theory. As stated in the previous paragraph, we assume that a correct description of the longitudinal and transverse characteristics of the perturbation source is, for a given longitudinal mode Σ,

$$(V+iU)_{\Sigma}(\rho,\eta)=\exp(-i\Sigma\eta)B(\rho) \; . \tag{17}$$

Σ is the dimensionless expression for the modulus of the longitudinal wave number associated with the longitudinal wavelength $\lambda_{\parallel}$; that is to say,

$$\Sigma=\frac{2\pi}{\alpha\lambda_{\parallel}} \; . \tag{18}$$

Note that the central mode value of Σ is $\frac{1}{4}$, since the central mode value of $\lambda_{\parallel}$ is $8\pi/\alpha$. We put $B(\rho)$ as the radial profile of the perturbation source, which is modelized by a material diaphragm of diameter $2\rho_{\pi}$:$B(\rho)=0$ for $0<\rho<\rho_{\pi}$ and $B(\rho)=-1$ for $\rho>\rho_{\pi}$. Then, the perturbation of the electric field can be expected to be of the following form:

$$e_{\Sigma}(\rho,\eta)=\exp(-i\Sigma\eta)f(\rho) \; , \tag{19}$$

in which $f(\rho)$ is the unknown transverse profile. Let us note that we have chosen to neglect the time dependence of the perturbation effect. We saw in the previous paragraph that this effect was concentrated at the tail of the pulse, and we assume that it does not depend on the time when it occurs. Replacing Eqs. (17) and (19) in Eq. (8), we obtain

$$\Delta_\rho f(\rho)+\frac{\Sigma}{F}f(\rho)=\frac{i}{F}B(\rho) . \tag{20}$$

One can recognize here the well known Helmholtz equation, which describes electromagnetic source radiations. We give in Appendix B a full theoretical treatment of Eqs. (17), (19), and (20), essentially based on the Green-function theory. Analytical calculations lead to the following solution for e_Σ (and complex conjugate):

$$e_\Sigma(\rho,\eta)=\frac{\exp[i(K\rho-\Sigma\eta)]}{F^{3/4}\Sigma^{1/4}}Z_K(\rho) , \tag{21}$$

in which

$$K=\left[\frac{\Sigma}{F}\right]^{1/2} \tag{22}$$

is the perturbation dimensionless transverse wave number. $Z_K(\rho)$ is an integral function that is given in Appendix B and exhibits no oscillating behavior.

The meaning of the relation (21) is obvious: electric-field transverse perturbations can propagate radially, in either an inward or an outward direction. This propagation regime is dispersive, since transverse and longitudinal wave numbers K and Σ depend on each other, according to Eq. (22).

C. Theoretical predictions

The dimensional form of the central mode transverse wavelength $\lambda_T=2\pi r_p/K$ is obtained directly from Eq. (22), in which Σ is replaced by its central mode value $\frac{1}{4}$, giving

$$\lambda_T=\left[\frac{4\pi\lambda}{\alpha}\right]^{1/2} . \tag{23}$$

Energy associated with a wave packet centered on the above main wavelength can be expected to propagate radially at the group velocity $V_g=\alpha r_p(d\Sigma/dK)$. We obtain $(d\Sigma/dK)=2\sqrt{\Sigma F}$ directly from Eq. (22), leading to the final form of V_g (with $\Sigma=\frac{1}{4}$),

$$V_g=\left[\frac{\alpha\lambda}{4\pi}\right]^{1/2} . \tag{24}$$

Considering a transverse wave packet propagating at the velocity V_g, whose source is located at r_π, and assuming that L_{foc} is the distance needed to reach the axis $r=0$, we obtain directly

$$L_{\text{foc}}=2\sqrt{\pi}\frac{r_\pi}{\sqrt{\alpha\lambda}} . \tag{25}$$

Since r_π is proportional to r_p, we can see that Eq. (25) is in perfect agreement with the numerical prediction of Sec. II B [(see Eq. (11)].

For a Gaussian beam of on-axis optical area Θ ($\Theta>\pi\sqrt{2}$), the exact relation between r_π and r_p is given by

$$\frac{r_\pi}{r_p}=\left[\frac{\log(\Theta/\pi)}{\log\sqrt{2}}\right]^{1/2} . \tag{26}$$

We can see that r_π and, accordingly, L_{foc}, increase with input-pulse on-axis area, in agreement with numerical results (since dimensionless Rabi frequency $\Omega\tau_p$ and optical area are equivalent).

The complexity of $Z_K(\rho)$ makes it impossible to carry out a general analytic calculation of $H_{\max}$ from Eq. (21). However, since $H_{\max}/H_0=(e_\Sigma+e_0)^2/e_0^2$ can be expected to be proportional to e_Σ/e_0 to first order (we put e_0 as the input reference dimensionless electric field), Eq. (21) leads to the following prediction:

$$\frac{H_{\max}}{H_0}\propto\frac{r_p^{3/2}\alpha^{3/4}}{\lambda^{3/4}} , \tag{27}$$

which corresponds well to the approximate numerical predictions that were made [see Sec. II, Eq. (12)]. Moreover, the parametric dependence of the focused-beam transverse size r_{foc} can be estimated from the prediction (27) by assuming that the full beam transmission rate is proportional to $(\alpha L_{\text{foc}})^{-1}$. This can be written

$$\frac{H_{\max}r_{\text{foc}}^2}{H_0r_p^2}\propto\frac{\lambda^{1/2}}{r_p\alpha^{1/2}} . \tag{28}$$

This gives clearly

$$\frac{r_{\text{foc}}}{r_p}\propto\frac{\lambda^{5/8}}{r_p^{5/4}\alpha^{5/8}} . \tag{29}$$

In the following section we demonstrate that this result corresponds closely to the experimental data.

IV. EXPERIMENTAL RESULTS

A. Atomic absorber and optical pulses

We used an atomic vapor of ^{169}Tm (nuclear spin $I=\frac{1}{2}$). In a 1-m-long oven, we obtained atomic concentrations from 0.45×10^{13} to 8×10^{13} at/cm^3, for temperatures ranging between 730 °C and 850 °C. ^{169}Tm was excited from the $J=\frac{7}{2}$ ground level to the $J=\frac{7}{2}$ state at 16 746.8 cm^{-1} ($\lambda=5971.26$ Å) with a mean electric dipole moment of 0.18 D. For the above-mentioned temperatures, Doppler line breadth is about 850 MHz and the spectral shift between the two main hyperfine components of the transition ($F=3\Longrightarrow F=3$ and $F=4\Longrightarrow F=4$) is about 1.45 GHz. The atomic level diagram and a numerical simulation of the spectral profile are shown in Fig. 10. We can note that the two hyperfine components are well separated. Because of this, we could center the laser frequency on either the $F=3$ or $F=4$ transition and thereby limit Zeeman degeneracy effects. Our optical pulses—of which the duration at half the maximum intensity was nearly 4 ns—originated from a single-mode cw dye Ar$^+$ pumped laser, amplified by a frequency doubled single mode YAG: Nd^{3+} source (YAG denotes yttrium aluminum garnet). Typical values of the input

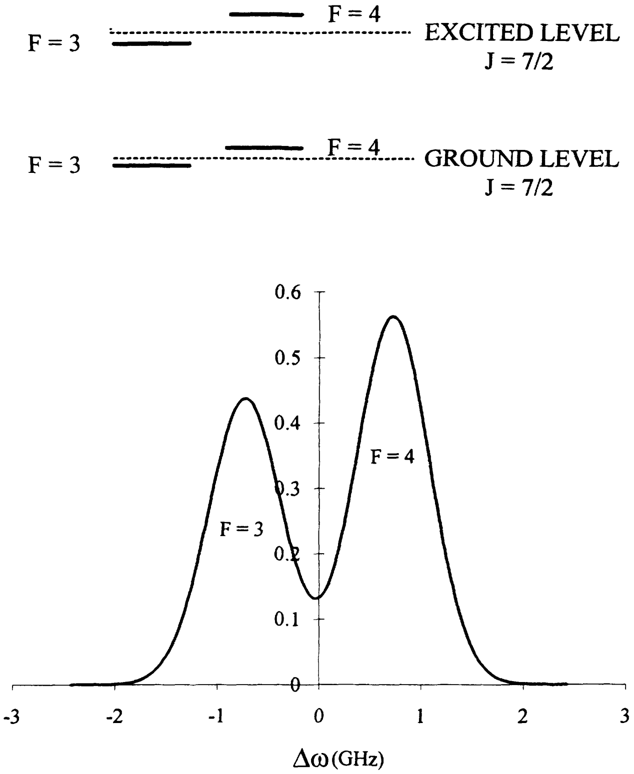

FIG. 10. Atomic level diagram and numerical simulation of the normalized spectral profile of the $\lambda = 5971.26$-Å fundamental transition of ^{169}Tm.

peak power ranged between 1 kW and 1 MW. Spatial filtering produced a fairly good Gaussian profile. The beam waist was located at the oven entrance and r_p was given six different values from nearly 0.25 to 1.7 mm by modifying the characteristics of a telescope. A lens imaged the output beam in front of either an IMACON 500 streak camera or a CCD video camera. As is shown in Sec. V B, the strongest LSSF effects do not systematically occur in strictly resonant interactions. The control of the detuning between laser and atomic resonance frequencies was carried out by making low-intensity absorption measurements in a second ^{169}Tm oven.

B. Comparison with theoretical predictions

Our aim was to confirm qualitatively the predicted dependencies of L_{foc}, r_{foc}, and $H_{\max}/H_0$ on r_p and N (but not on λ, since it could not be changed experimentally). L_{foc} having been defined as fixed and equal to the oven length (1 m), r_p and N had to vary while $r_p/\sqrt{N}$ (that is to say, L_{foc}) had to be constant. It is interesting to express theoretical predictions (27) and (29) by taking this condition into account. This produces, respectively,

$$\frac{H_{\max}}{H_0} \propto r_p^3 \tag{30}$$

and

$$\frac{r_{\text{foc}}}{r_p} \propto \frac{1}{r_p^{5/2}} . \tag{31}$$

As far as $H_{\max}/H_0$ is concerned, the prediction (30) will systematically lead to an overestimation of experimental measurements. This overestimation can be readily explained by taking into account what we call the "residual absorption" induced by Zeeman degeneracy, of which a detailed discussion is given in Sec. V A (although it has been omitted in the theoretical part of this work for the sake of simplicity). The chief point is that, independently of any transverse effect, Zeeman degeneracy may hinder ideal SIT (propagation with practically no absorption). In such a case, transverse perturbations are not as "efficient" as in nondegenerate media, since they have undergone absorption. It follows that predictions about $H_{\max}/H_0$ must be tempered proportionally to the optical thickness of the medium (that is to say, by αL_{foc}). Thus, we obtain new predictions extended to degenerate situations,

$$\frac{H_{\max}}{H_0} \propto r_p , \tag{32}$$

and

$$\frac{r_{\text{foc}}}{r_p} \propto \frac{1}{r_p^{3/2}} . \tag{33}$$

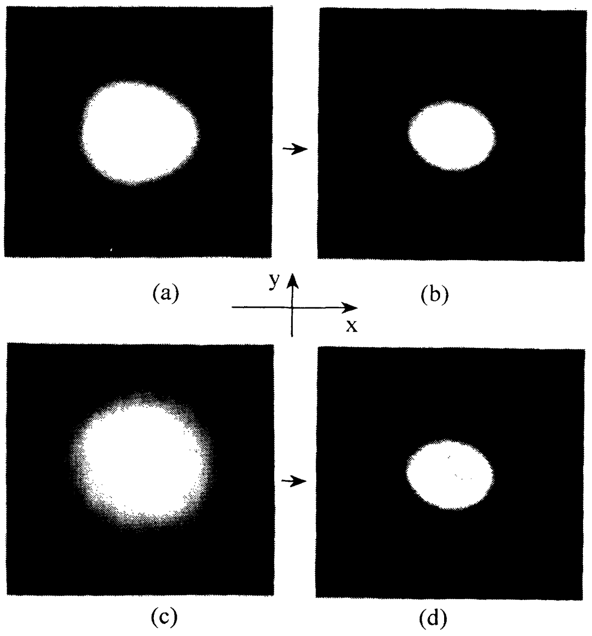

FIG. 11. Dependence of LSSF phenomena on the beam's transverse size. Video camera outputs. (a) Input pulse whose r_p is 0.03 cm. (b) Output focused pulse corresponding to (a), $N = 2.0 \times 10^{13}$ at/cm^3. (c) Input pulse whose r_p is 0.07 cm. (d) Output focused pulse corresponding to (c), $N = 7.0 \times 10^{13}$ at/cm^3. On-axis optical areas of the input pulses were nearly 5π, and the maximum focusing (corresponding to the above atomic concentrations) was obtained when the laser frequency was tuned to the $F = 3$ hyperfine component of the atomic line.

LSSF had been observed for r_p ranging between 0.3 and 0.9 mm. For the sake of example, input and focused output beams are compared in Fig. 11, for $r_p = 0.3$ and 0.7 mm. Corresponding atomic concentrations are, respectively, $N = 2\times10^{13}$ and 7×10^{13} at/cm^3, corresponding closely to theoretical predictions about L_{foc}. It is noteworthy that r_{foc}/r_p can be predicted from (33) to be about 3.5 times smaller in the case (c)$\Longrightarrow$(d) than in the case (a)$\Longrightarrow$(b), which obviously tallies closely with experimental data.

Measured values of $H_{\max}/H_0$ were nearly 1.4 and 3.8, respectively, for (a)$\Longrightarrow$(b) and (c)$\Longrightarrow$(d), (that is, 2.7 times larger in the second case than in the first, even though (32) would have predicted 2.3 times). In Fig. 11, the input on-axis value of the optical area was, in each case, about 5π. Streak camera outputs corresponding respectively to Figs. 11(c) and 11(d) are presented in Figs. 12(a) and 12(b). One can note that temporal reshaping leading to the formation of successive 2π pulses does not occur, confirming our predictions (see Sec. II C). Such reshaping was observed for r_p larger than 0.9 mm, but in these cases LSSF was progressively replaced by small-scale self-focusing. This means that energy transverse profiles degenerate into a hot-spots pattern and that streak camera images exhibit filamentary structures.

As far as parametric dependences are concerned, theoretical predictions eventually proved to be correct in the case of LSSF, but these dependences seemed to be different in the case of small-scale self-focusing than they are in LSSF. As for numerical predictions in cylindrical symmetry, we saw that they failed to hold true for small values of F: LSSF was predicted and small-scale self-focusing was observed.

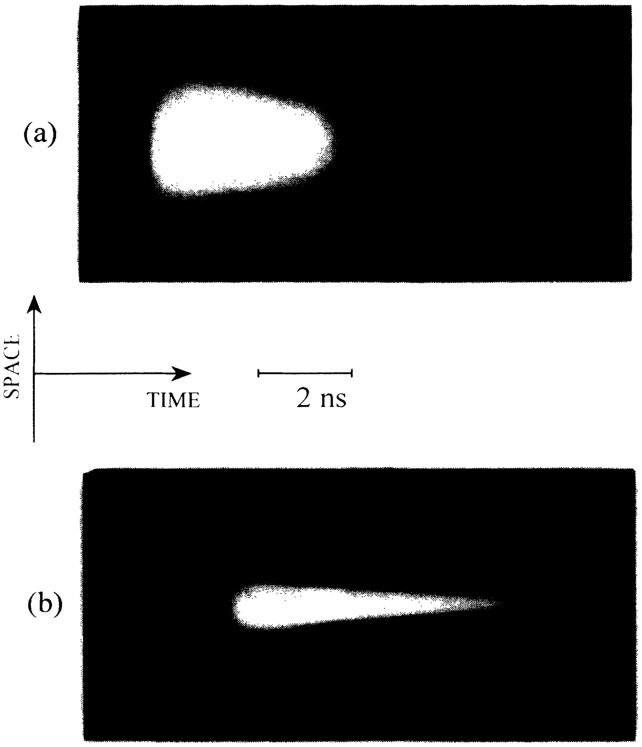

FIG. 12. Characteristic evolution of the intensity spatiotemporal profile in a case of LSSF. Streak camera outputs. (a) and (b) were obtained, respectively, for the input and output on-resonance pulses corresponding to illustrations (c) and (d) of Fig. 12.

V. COMPLEMENTARY DISCUSSIONS

A. Zeeman degeneracy effects

Slusher and Gibbs [18] could experimentally investigate SIT in ideal nondegenerate media by placing a rubidium cell in a magnetic field. Numerous authors were also interested in the effects of Zeeman degeneracy on SIT phenomena. Rhodes and Szöke [14], followed later by Zembrod and Gruhl [15] and Gibbs, McCall, and Salamo [16] studied these effects in SF$_6$, and showed that SIT may occur even in a highly degenerate medium. Salamo, Gibbs, and Churchill [30] and Krieger, Gaida, and Toschek [17] investigated SIT in less degenerate atomic media (respectively, in Na and Ne). They showed that the main characteristic features of SIT (such as temporal reshaping and dependence of energy transition rate on input area), although they existed, may be significantly altered by degeneracy. Global absorption of the beam is greater in degenerate than in nondegenerate media, and although this does not necessarily involve qualitative changes in self-focusing theoretical predictions, quantitative changes can be expected, as was shown in Sec. IV B. A simple interpretation of these effects follows logically from a few short numerical results that we shall demonstrate. Let us recall the expression of the atomic polarization absorptive component $v(t)$ [Eq. (15a)],

$$v(t) = -\sum_i p_i \sin\theta_i(t) , \tag{34}$$

in which $\theta_i(t)$ is the partial optical area associated with the ith dipole moment of statistical weight p_i. One can see that the simple periodic oscillating polarization behavior in an ideal (that is, nondegenerate) medium could be replaced by a superposition of oscillating behaviors. Global population transfers may become impossible [31]. One can easily understand that the usual picture of a 2π pulse (in which 2π is the optical area associated with a unique characteristic dipole moment, which is obviously meaningless in a degenerate medium), propagating without attenuation by driving the atomic system first from the ground state to the excited state and then back to the ground state, might be quite inaccurate. In a degenerate medium, the same input pulse generally undergoes what we call residual absorption. Indeed, a significant part of the atomic population is left in the excited state after its crossing, whatever the propagation distance is, that is, in spite of temporal reshaping. The expected differences between the temporal reshaping effects occurring respectively in an ideal and in a degenerate medium are illustrated qualitatively by the results given in Fig. 13.

The degenerate transition is $F=3 \Longrightarrow F=3$ in linear polarization, and the "ideal" transition dipole moment is

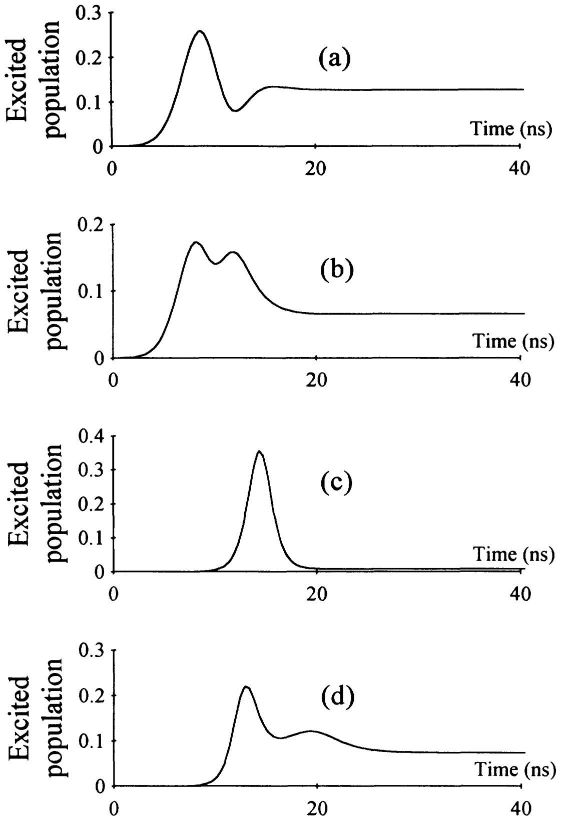

FIG. 13. Temporal evolution of the excited atomic population at $z=0$ and $z=20$ cm: comparison between ideal nondegenerate and degenerate $F=3 \Longrightarrow F=3$ (linear polarization) cases. (a) Ideal case, $z=0$. (b) Degenerate case, $z=0$. (c) Ideal case, $z=20$ cm. (d) Degenerate case, $z=20$ cm. In the degenerate case, one can see that a significant part of the atomic population remains in the excited state after the pulse crossing at $z=20$ cm, that is, in spite of temporal reshaping ($L_{\mathrm{res}} \ll 20$ cm). The pulse undergoes residual absorption.

taken to be equal to the quadratic mean value of the degenerate transition dipole moments. The time evolution of the excited population is compared at the input plane and at $z=20$ cm, in both ideal and degenerate cases, for an input 2.6π pulse. At $z=0$, nearly 13% of the atomic ideal population (a) and 7% of the degenerate one (c) are left in the excited state. At $z=20$ cm, excited populations are 1% (b) and 7% (d). This means that residual absorption remains in the degenerate medium, in spite of temporal reshaping. Considerable qualitative changes are induced in the self-focusing main features, as is shown in Fig. 14, in which the corresponding on-axis energy-density longitudinal evolutions are compared. $H_{\max}$ is much smaller in the degenerate case (b) than it is in the ideal one (a). When one remembers that the concept of optical area is involved in the theoretical prediction of L_{foc} [see its dependence on r_π in Eq. (25)], the small change between (b) and (a) can readily be understood. As for the parametric dependence that we obtained theoretically, numerical simulations showed that they remain valid even when Zeeman degeneracy is taken into account.

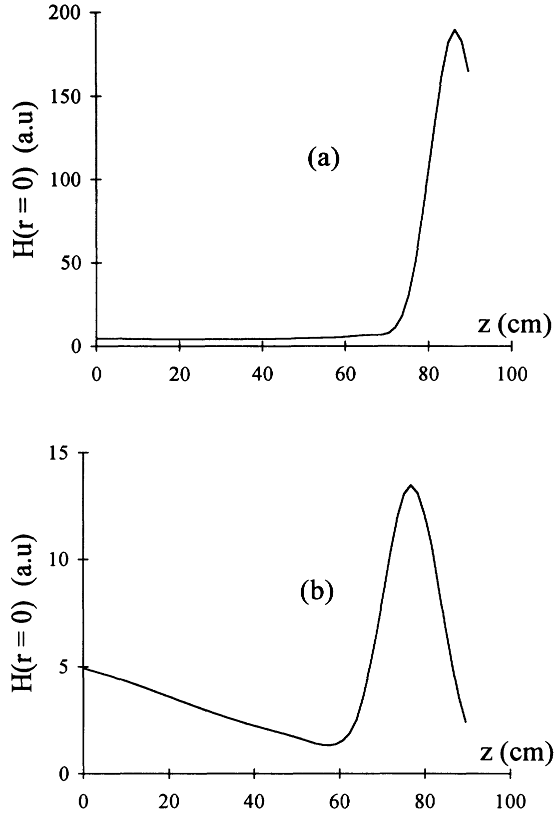

FIG. 14. Compared longitudinal evolutions of the on-axis energy densities in both the ideal and degenerate cases. Influence of the residual absorption on LSSF. (a) Ideal case. (b) Degenerate $F=3$ case. (Note different vertical scales.)

Only the absolute value of L_{foc}, $H_{\max}/H_0$, and r_{foc}/r_p depends on the particular degeneracy.

B. Dispersive effects

The in-quadrature component U of the macroscopic polarization describes "dispersive" effects that may be re-

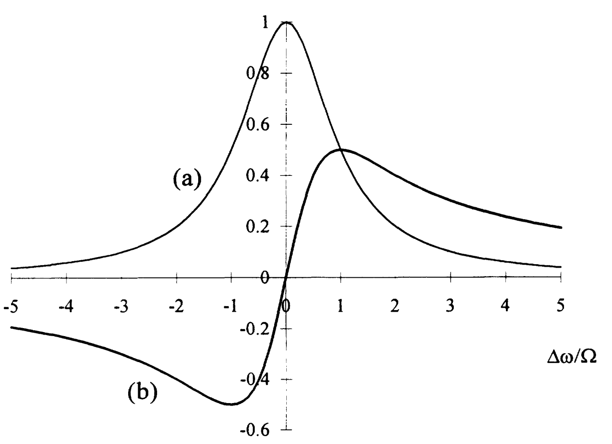

FIG. 15. A plot of the amplitudes of the "in-phase" v (a) and "in-quadrature" u (b) components of the atomic polarization. The case of an incident rectangular pulse.

sponsible for self-focusing or self-defocusing. We have not dealt with these effects up to now, since they do not occur at the exact resonance ($U=0$, as was shown in Sec. II). Self-focusing on the "red" side of the atomic resonance was first investigated by Grichkowsky and Armstrong [32] in the adiabatic-approximation regime [33], that is, when the detuning from resonance is much larger than the Rabi frequency (no absorption is expected in these conditions). The adiabatic formalism is equivalent to first order to that of nonlinear susceptibilities. An intensity-dependent index of refraction is enough to explain the self-lensing mechanism that led to focusing phenomena. We have been interested in studying the effects that occur at smaller detunings and, in particular, the detunings that are of the order of magnitude of the Rabi frequency. Solutions of the Bloch equations [see Sec. II, Eq. (5)] can be derived analytically for an input rectangular pulse [24] (whatever the detuning is), producing

$$\begin{aligned} u(\Delta\omega,t) &= \frac{\Omega\Delta\omega}{\Omega_r^2}(1-\cos\Omega_r t)\,, \\ v(\Delta\omega,t) &= -\frac{\Omega}{\Omega_r}\sin\Omega_r t\,, \\ w(\Delta\omega,t) &= -\frac{\Delta\omega^2+\Omega^2\cos\Omega_r t}{\Omega_r^2}\,, \end{aligned} \tag{35}$$

in which Ω_r is the generalized Rabi frequency defined by $\Omega_r=\sqrt{\Omega^2+\Delta\omega^2}$. The profiles of the amplitudes of u and v are given in Fig. 15. One recognizes the characteristic spectral dependence of the real and imaginary parts of atomic linear susceptibility in the stationary regime [34]. It is this that can explain lens effects. The solutions (35) show that although lens effects are superimposed on transient behaviors, they are expected to occur even in the "small-detuning" regime. This was checked experimentally on both sides of the atomic resonance. Self-defocusing occurs on the red side, whereas self-focusing, as is shown in Fig. 16, occurs on the blue side. Illustration (a) represents the input or nonresonant beam. Illustration (b) demonstrates a strong focusing and was obtained for a "blue" detuning of the order of Ω_0. On exact resonance, the pulse was strongly absorbed, as is shown by illustration (c). This experiment confirmed the possibility of lens effects leading to self-focusing or defocusing in the case of detunings smaller than those of the adiabatic regime (that is, in absorbant media).

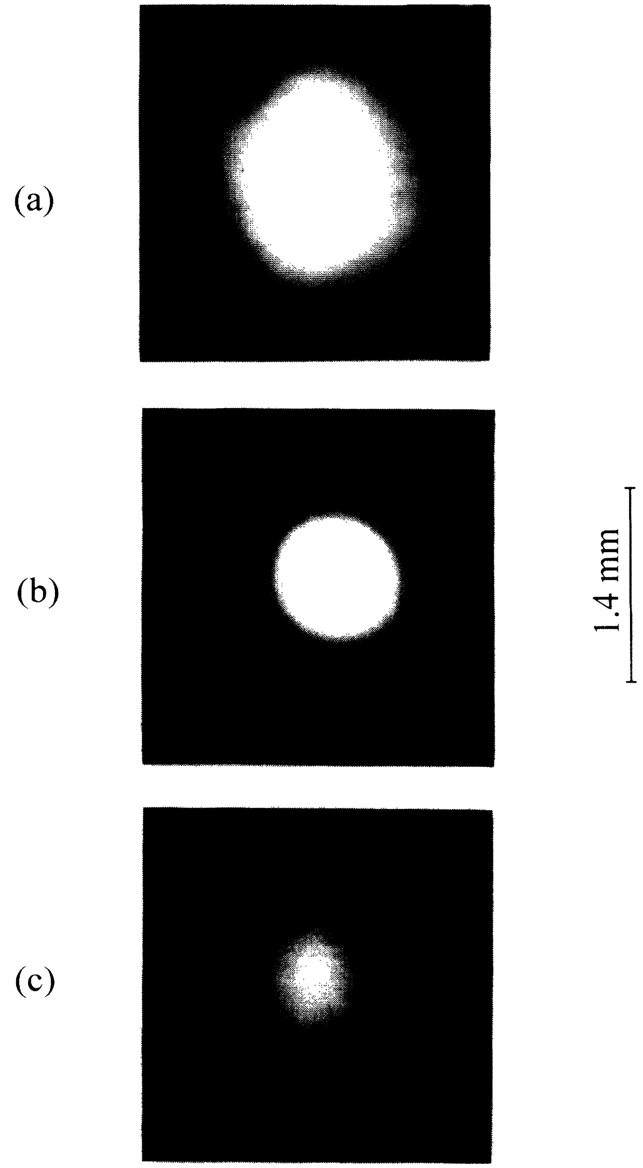

FIG. 16. Lenslike effect in coherent resonant self-focusing. Video camera outputs. (a) Input pulse. (b) Focusing when detuning is nearly equal to the Rabi frequency, on the blue side of the atomic line. (c) When the laser frequency was tuned on-resonance, focusing disappeared and the pulse underwent only absorption.

VI. SUMMARY

We now have a quantitative theoretical model for coherent on-resonance LSSF. Theoretical predictions concerning the parametric dependences of the focusing distance L_{foc}, and the ratios of the on-axis energy densities and pulse transverse sizes between the focus and the input plane, respectively, $H_{\max}/H_0$ and r_{foc}/r_p, have been shown to correspond closely to numerical simulations and experimental results. The parametric dependence of L_{foc} on the input pulse peak power is quite different from that which can be obtained in the usual nonlinear case [2]. The relative predominance of either the LSSF or SIT phenomenon is characterized by the parameter $\sqrt{F}$. We have seen that when the LSSF dominates, some basic characteristics of plane-wave SIT such as pulse breakup and large delays can be significantly altered. We limited our study to cases in which the pulse spectral width was either smaller than or of the same scale as the Doppler-broadened line width ($D>1$). In such cases the effective linear absorption of the pulses can be much larger in degenerate media than it is in nondegenerate ideal media. As a result, the relative importance of LSSF phenomena (due to the strong absorption superimposed) can be reduced considerably. We have seen that dispersive effects, which do not play a major role in coherent on-resonance phenomena, appear to be preponderant for detunings of the order of magnitude of the initial pulse peak Rabi frequency. Numerical simulations assuming cylindrical symmetry, which predict LSSF even for small values of F, obviously do not correspond to experimental results because small-scale self-focusing is observed in such cases.

APPENDIX A

Since we saw that L_{foc} is proportional to r_p, we can assume that

$$L_{\text{foc}} \propto r_p \alpha^n \lambda^m \; . \tag{A1}$$

It follows from Eq. (8) of Sec. II that if we consider a variation of α, λ, and r_p in which $F=\lambda/(4\pi\alpha r_p^2)$ is constant, the dimensionless focusing distance

$$\eta_{\text{foc}}=\alpha L_{\text{foc}} \tag{A2}$$

is also constant. Let us assume that α and λ are, respectively, multiplied by x and y, and that F is constant. It implies that r_p is multiplied by a factor $\sqrt{y}/\sqrt{x}$. It follows from Eq. (A2) that L_{foc} is divided by x, and from Eq. (A1) that it is multiplied by $\sqrt{y}/\sqrt{x}\,(x^n y^m)$, which finally requires that

$$n=m=-\tfrac{1}{2} \; . \tag{A3}$$

APPENDIX B

The solution of Eq. (20) can be derived from the Green-functions theory and the elementary Helmholtz equation defined by

$$\Delta_\rho s(\rho)+K^2 s(\rho)=\delta \; , \tag{B1}$$

in which K satisfies Eq. (22) and where δ is the Dirac function. δ can be viewed as a perturbation source located at $r=0$. The general solution $s(\rho)$ of Eq. (B1) is a linear complex combination of the first-order Hankel function $H_0^{(1)}$ and its complex conjugate [35]. $H_0^{(1)}$ can be written as follows:

$$H_0^{(1)}(K\rho)=\frac{\exp(iK\rho)}{\sqrt{K\rho}}M(K\rho) \; , \tag{B2}$$

in which $M(K\rho)$ is defined by

$$M(K\rho)=\left[\frac{2}{\pi}\right]^{1/2}\frac{\exp(-i\pi/4)}{\Gamma(1/2)}\int_0^\infty\left[1+\frac{it}{K\rho}\right]^{-1/2} \times t^{-1/2}\exp(-t)\,dt \; , \tag{B3}$$

in order to recall that $H_0^{(1)}$ is known [36] to behave asymptotically like $\exp(iK\rho)/\sqrt{K\rho}$. Γ is the well known gamma function.

Because of the linearity of Eq. (20) with respect to the perturbation source $(1/F)B(\rho)$, one can consider that $B(\rho)$ is a superposition of local Dirac perturbations. Putting $G(\rho,x)$ as the solution of Eq. (B1) corresponding to a Dirac perturbation located at x (G is usually called the Green function of the problem), we obtain the general solution of Eq. (20),

$$f(\rho)=\frac{i}{F}\int_{D_x}G(\rho,x)B(x)\,dx \; , \tag{B4}$$

in which D_x is the perturbation source domain [$B(x)$ is equal to zero outside of D_x]. One can derive a simpler analytic form for $f(\rho)$. Indeed, we know that $G(\rho,x)=G(\rho-x,0)$ since the Laplacian operator Δ_ρ is translation invariant. Now $G(\rho-x,0)$ is exactly $s(\rho-x)$, since it corresponds to the response to a Dirac perturbation located at $r=0$. Therefore, $G(\rho,x)$ is a linear combination of $H_0^{(1)}[K(\rho-x)]$ and its complex conjugate [see Eqs. (B2) and (B3)]. Then it follows from Eq. (B4) that $f(\rho)$ is a linear combination of $f_1(\rho)$ (and its complex conjugate) defined by

$$f_1(\rho)=\frac{\exp(iK\rho)}{F\sqrt{K}}Z_K(\rho) \; , \tag{B5}$$

in which

$$Z_K(\rho)=i\int_{D_x}\frac{\exp(-iKx)M[K(x-\rho)]}{\sqrt{x-\rho}}B(x)\,dx \; . \tag{B6}$$

Replacing Eq. (B5) in Eq. (19), one obtains directly the solution (21) for the electric-field perturbation.

---

[1] R. Y. Chiao, E. Garmire, and C. H. Townes, Phys. Rev. Lett. **13**, 479 (1964).

[2] P. L. Kelley, Phys. Rev. Lett. **15**, 1005 (1965).

[3] A. Javan and P. L. Kelley, IEEE J. Quantum Electron. **QE-2**, 470 (1966).

[4] S. A. Akhmanov, A. P. Sokhurov, and R. V. Khokhlov, *Laser Handbook*, edited by F. Arrechi (North-Holland, Amsterdam, 1972), Chap. E3.

[5] D. J. Harter and R. W. Boyd, Phys. Rev. A **29**, 739 (1984).

[6] E. Braun, L. P. Faucheux, and A. Libchaber, Phys. Rev. A **48**, 611 (1993).

[7] Y. R. Shen, *The Principles of Nonlinear Optics* (Wiley, New York, 1984).

[8] G. K. L. Wong and Y. R. Shen, Phys. Rev. Lett. **32**, 527 (1974).

[9] E. G. Hanson, Y. R. Shen, and G. K. L. Wong, Opt. Commun. **20**, 45 (1977).

[10] M. G. Boshier and W. J. Sandle, Opt. Commun. **42**, 371 (1982).

[11] K. Tai, H. M. Gibbs, M. C. Rushford, N. Peyghambarian, J. S. Satchell, M. G. Boshier, R. J. Ballagh, W. J. Sandle, M. LeBerre, E. Ressayre, A. Tallet, J. Teichmann, Y. Claude, F. P. Mattar, and P. D. Drummond, Opt. Lett. **9**, 243 (1984).

[12] M. LeBerre, E. Ressayre, A. Tallet, F. P. Mattar, J. Opt. Soc. Am. B **2**, 956 (1985).

[13] S. L. McCall and E. L. Hahn, (a) Phys. Rev. Lett. **18**, 908 (1967); (b) Phys. Rev. **183**, 457 (1969).

[14] C. K. Rhodes and A. Szöke, Phys. Rev. **184**, 25 (1969).

[15] A. Zembrod and Th. Gruhl, Phys. Rev. Lett. **27**, 287 (1971).

[16] H. M. Gibbs, S. L. McCall, and G. J. Salamo, Phys. Rev. A **12**, 1032 (1975).

[17] W. Krieger, G. Gaida, and P. E. Toschek, Z. Phys. B **25**, 297 (1976).

[18] R. E. Slusher and H. M. Gibbs, Phys. Rev. A **5**, 1634 (1972).

[19] N. Wright and M. C. Newstein, Opt. Commun. **9**, 8 (1973).

[20] H. M. Gibbs, B. Bölger, F. P. Mattar, M. C. Newstein, G. Forster, and P. E. Toschek, Phys. Rev. Lett. **37**, 1743 (1976).

[21] F. P. Mattar, Appl. Phys. **17**, 53 (1978).

[22] F. P. Mattar and M. C. Newstein, Comp. Phys. Commun. **20**, 139 (1980).

[23] See, for instance, P. W. Milonni and J. H. Eberly, *Lasers* (Wiley, New York, 1988), Chap. 8.

[24] See, for instance, L. Allen and J. H. Eberly, *Optical Resonance and Two-Level Atoms* (Wiley, New York, 1975).

[25] M. Lax, W. H. Louisell, and W. B. Knight, Phys. Rev. A **11**, 1365 (1975).

[26] B. W. Shore, Opt. Commun. **37**, 92 (1981).

[27] G. L. Lamb, Jr., *Elements of Soliton Theory* (Wiley, New York, 1980).

[28] Ph. Kupecek, M. Comte, J. P. Marinier, J. P. Babuel-Peyrissac, and C. Bardin, Opt. Commun. **65**, 306 (1988).

[29] J. W. Lit and R. Tremblay, J. Opt. Soc. Am. **59**, 359 (1969).

[30] G. J. Salamo, H. M. Gibbs, and G. G. Churchill, Phys. Rev. Lett. **33**, 273 (1974).

[31] B. W. Shore, Phys. Rev. A **17**, 1739 (1978).

[32] D. Grischkowsky and J. A. Armstrong, Phys. Rev. A **6**, 1566 (1972).

[33] See, for a detailed derivation of the approximation, (a) M. D. Crisp, Phys. Rev. A **8**, 2128 (1973); (b) M. E. Crenshaw and C. D. Cantrell, *ibid.* **37**, 3338 (1988); and for a numerical study of self-focusing in the adiabatic regime, (c) M. E. Crenshaw and C. D. Cantrell, Opt. Lett. **13**, 386 (1988).

[34] See Yariv's work of reference on the subject, for example, A. Yariv, *Quantum Electronics,* 2nd ed. (Wiley, New York, 1975), Chap. 8.

[35] R. Dautray and J. L. Lions, *Analyse Mathematique pour les Sciences et Techniques* (Masson, Paris, 1988). See the chapter on the Laplacian operator.

[36] *Handbook of Mathematical Functions,* edited by M. Abramowitz and I. Stegun (Dover, New York, 1972).

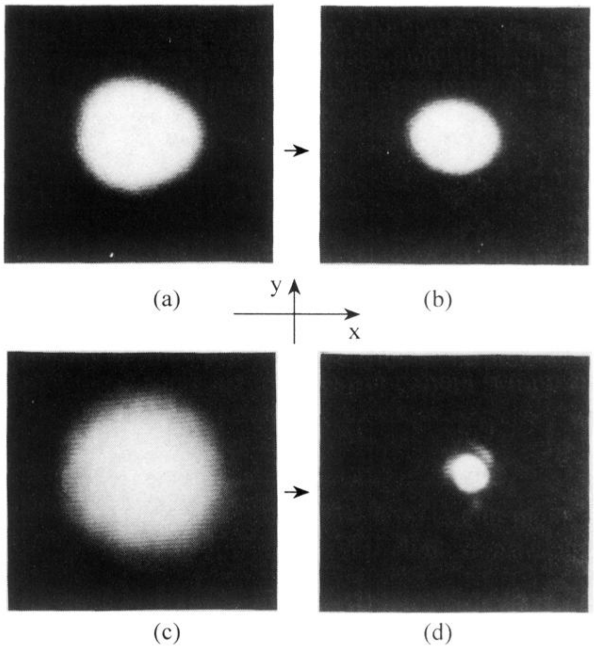

FIG. 11. Dependence of LSSF phenomena on the beam's transverse size. Video camera outputs. (a) Input pulse whose r_p is 0.03 cm. (b) Output focused pulse corresponding to (a), $N=2.0\times10^{13}$ at/cm^3. (c) Input pulse whose r_p is 0.07 cm. (d) Output focused pulse corresponding to (c), $N=7.0\times10^{13}$ at/cm^3. On-axis optical areas of the input pulses were nearly 5π, and the maximum focusing (corresponding to the above atomic concentrations) was obtained when the laser frequency was tuned to the $F=3$ hyperfine component of the atomic line.

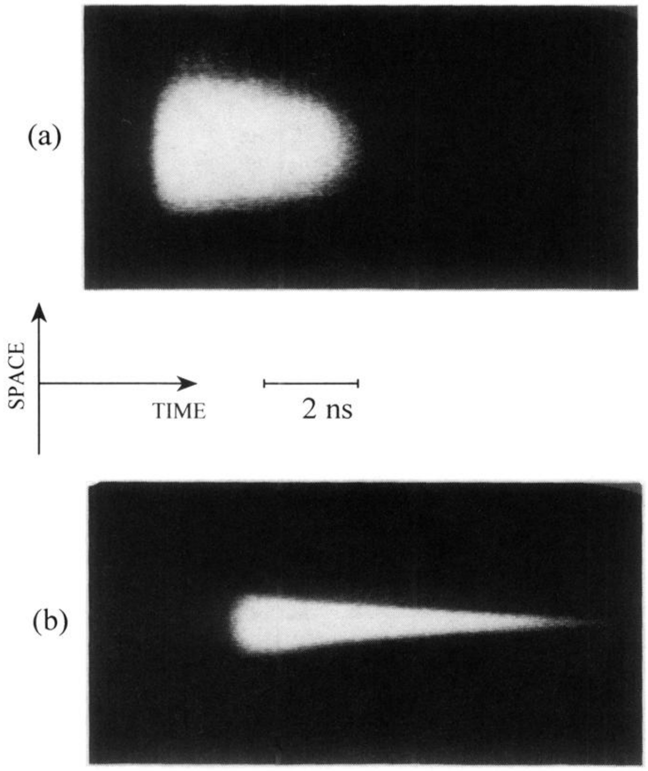

FIG. 12. Characteristic evolution of the intensity spatiotemporal profile in a case of LSSF. Streak camera outputs. (a) and (b) were obtained, respectively, for the input and output on-resonance pulses corresponding to illustrations (c) and (d) of Fig. 12.

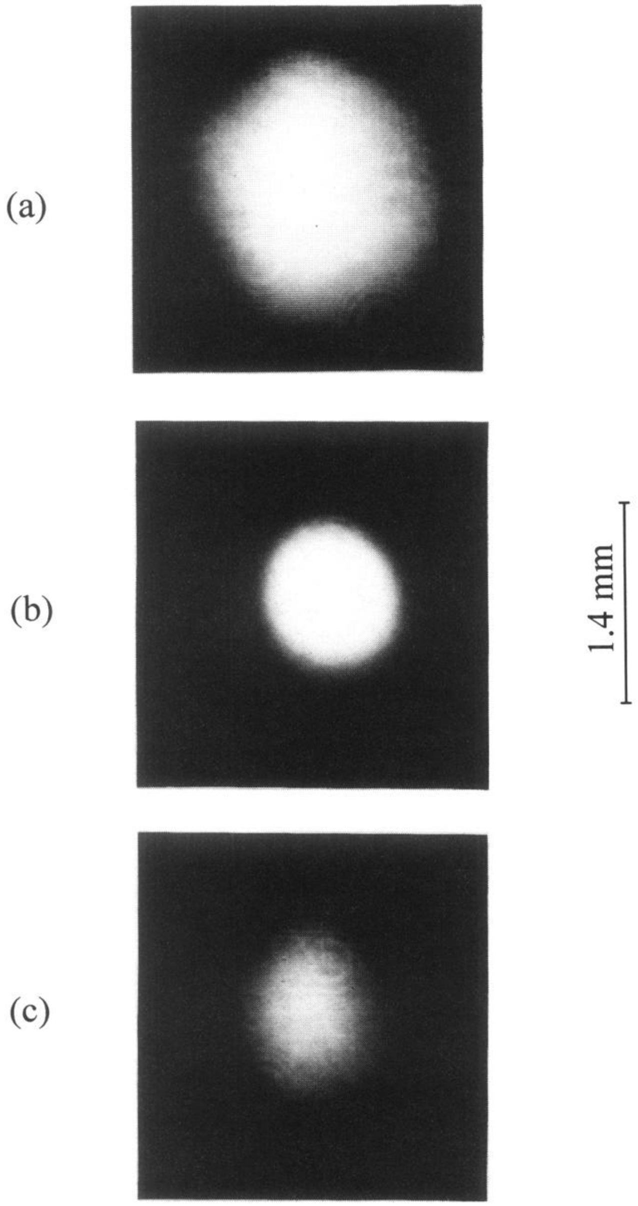

FIG. 16. Lenslike effect in coherent resonant self-focusing. Video camera outputs. (a) Input pulse. (b) Focusing when detuning is nearly equal to the Rabi frequency, on the blue side of the atomic line. (c) When the laser frequency was tuned on-resonance, focusing disappeared and the pulse underwent only absorption.